Li Metal Batteries Hot Paper

How to cite: *Angew. Chem. Int. Ed.* **2023,** *62,* e202217081
International Edition: doi.org/10.1002/anie.202217081
German Edition: doi.org/10.1002/ange.202217081

Halide Layer Cathodes for Compatible and Fast-Charged Halides-Based All-Solid-State Li Metal Batteries

*Jianwen Liang[+], Xiaona Li[+], Jung Tae Kim, Xiaoge Hao, Hui Duan, Ruying Li, and Xueliang Sun**

Abstract: Insertion-type compounds based on oxides and sulfides have been widely identified and well-studied as cathode materials in lithium-ion batteries. However, halides have rarely been used due to their high solubility in organic liquid electrolytes. Here, we reveal the insertion electrochemistry of VX_3 (X = Cl, Br, I) by introducing a compatible halide solid-state electrolyte with a wide electrochemical stability window. X-ray absorption near-edge structure analyses reveal a two-step lithiation process and the structural transition of typical VCl_3. Fast Li^+ insertion/extraction in the layered VX_3 active materials and favorable interface guaranteed by the compatible electrode-electrolyte design enables high rate capability and stable operation of all-solid-state Li-VX_3 batteries. The findings from this study will contribute to developing intercalation insertion electrochemistry of halide materials and exploring novel electrode materials in viable energy storage systems.

Rechargeable Li-ion batteries (LIBs) based on intercalation chemistry have become a premier technology that can satisfy the increasing demand for energy storage systems with high energy density.[1] The discovery, design, and deep fundamental understanding of intercalation cathode materials has played a major role in promoting the development of LIBs in terms of their performance, safety, and sustainability. Starting from the study of layered TiS_2 in the 1970s,[2] most intercalation materials with open frameworks have been well investigated in LIBs and great success has been achieved with high-voltage layered oxides, such as conventional $LiCoO_2$ cathodes. However, compared to oxides and chalcogenides, the lithiation/delithiation properties of intercalation-type metal halides have been rarely investigated.[3]

[*] Dr. J. Liang,[+] Dr. X. Li,[+] J. T. Kim, X. Hao, Dr. H. Duan, R. Li, Prof. X. Sun
Department of Mechanical and Materials Engineering, University of Western Ontario
1151 Richmond St, London, Ontario, N6A 3K7 (Canada)
E-mail: xsun9@uwo.ca

[+] These authors contributed equally to this work.

The metal halide families are indeed promising electrode materials for LIBs. The theoretical capacity of metal halides can be as high as several hundred $mAh\,g^{-1}$, due to the multivalent nature of the metals.[4] Moreover, their lithiated states (Li_aMX_b) have high lithium-ion conductivities, further making them attractive.[4b,5] While they exhibit high solubility in liquid electrolytes, making them difficult to be used in traditional LIBs. For example, the dissolution of conversion-type metal halide electrodes (MX_n, M: Fe, Cu, Ni, etc., and X: F, Cl, and Br) in conventional organic liquid electrolytes and high-temperature molten salt electrolytes has been well reported.[6] Since the active species are involved in the reactions with the electrolyte component during lithiation/delithiation, complicated electrochemical behaviour and poor performance is always an issue.

The compatibility between electrode materials and electrolytes is one of the main obstacles hindering the development of LIBs.[7] With the discovery of different electrodes, state-of-the-art electrolytes have been tailored and developed to meet the specific requirements of the electrodes. Many new electrolyte systems are designed to support and facilitate progress in the development of new battery chemistries. For example, Wang et al. reported a halogen conversion-intercalation chemistry in graphite enabled by water-in-salt electrolytes.[8] Zhou et al. promoted new polyiodide-based chemistry by adopting a designed hybrid electrolyte composed of a dispersion poly(ethylene oxide) layer and a blocking $Li_{1.5}Al_{0.5}Ge_{1.5}(PO_4)_3$ layer.[9] Both the electrochemical window of the electrolytes and the stability toward electrode materials play crucial roles in designing stable electrode-electrolyte interfaces to enable reliable battery systems. Thus, when seeking appropriate electrolytes for intercalation-type metal halide electrodes, halide-based solid-state electrolytes (SSEs) stand out among the numerous electrolyte systems.[10] They possess high ionic conductivity (not for fluorides),[11] good air stability,[12] and deformability.[13] Remarkably, chloride-based SSEs can also achieve relatively wide electrochemical stability windows compared to traditional liquid electrolytes, polymer-based, or sulfide-based electrolytes. Moreover, as both electrolyte and electrode materials are based on halides, the electrode-electrolyte interfacial stability can be achieved in a thermodynamic manner instead of a passivation process.

With consideration of the aforementioned demands and features, taking VX_3 as an example, we have successfully developed a novel lithium intercalation chemistry in layered halide electrode materials enabled by compatible halide SSEs. With high ionic conductivities and wide electro-

chemical stability windows, halide SSEs are the perfect candidates for VX_3 electrodes. The problem of the high solubility of VX_3 in liquid organic solvents can be completely eliminated in a solid-state configuration. There are also no side reactions between VX_3 electrodes (including the lithiated species) and halide SSEs. Because of the fast Li^+ migration within the VX_3 layered skeleton and favorable electorde-electrolyte interface, we have achieved the fabrication of all-solid-state Li-VX_3 batteries with an extremely high rate, high loading, and stable cycling performance. We hope that the carefully designed combinations of the electrode and electrolyte materials will contribute to developing new intercalation chemistries beyond traditional oxides and sulfides and discovering novel electrode materials suitable for ASSBs with high energy density and unparalleled safety.

The redox energies of the V^{2+}/V^{3+} couple in layered VX_3 (X = V, Br, and I) compounds with the influence of the anions are illustrated in Figure 1a. The lithiation/delithiaiton plateaus of the VX_3 electrode are highly related to the halide anions and the highest potential is achieved in VCl_3 with the most electronegative Cl^-. The typical Cl *3p*-V *4d* hybridization in VCl_3 is illustrated in the molecular orbital energy diagram (Figure 1b), giving the redox potential around 3 V (vs. Li^+/Li) for the V^{2+}/V^{3+} couple. Inspired by these considerations, we first analyzed the structural chemistry of the V-based chloride components VCl_3 and $LiVCl_3$, which illustrates the halogen intercalation chemistry and the host structure evolution during Li insertion/extraction. As presented in Figure 1c, layered VX_3 has the common BiI_3 structure where the hexagonal-closed-packed (hcp) halide framework with V^{3+} occupies the octahedral holes. The edge-shared VX_6 octahedra are stacked in an AB sequence (O1-type structure, *R*-3 space group) along the *c* direction and there is relatively weak Van der Waals interaction between the interlayers. VCl_3 is thermodynamically stable at room temperature and is widely used to prepare other vanadium complexes. To examine the electrochemical application of the VCl_3 in all-solid-state batteries, we directly use commercially available polycrystalline powder with bulk and micro-structures (Figure S1). Rietveld analysis of the synchrotron X-ray diffraction (XRD) patterns confirmed the existence of a pure single phase (Figure 1e), with space group and lattice parameters that denote a VCl_3 structure (JCPDS no. 01-077-0203) from the database without additional V or Cl vacancy. Theoretically, the lithiation of layered VCl_3 involves one-electron transfer per molecular, with $LiVCl_3$ as the fully lithiated species corresponding to a theoretical capacity of 170 mAh g^{-1}.

To gain insights into the insertion chemistry and the structure of the lithiated species, $LiVCl_3$ was synthesized and analyzed as a theoretical product. The detailed synthesis process of $LiVCl_3$ is provided in the Supporting Information. The fully lithiated state of $LiVCl_3$ possesses the O3 layered structure with an *R*-3*m* space group as presented in Figure 1d. The Rietveld XRD (Figure 1f, Table S1,2) demonstrates that both the V and Li sites are located in the center of Cl6 octahedron. No Li or V atoms in tetrahedral sites have been found. We also carried out the cation distribution by refining Li and V on the alkali metal, 3*b*, and transition

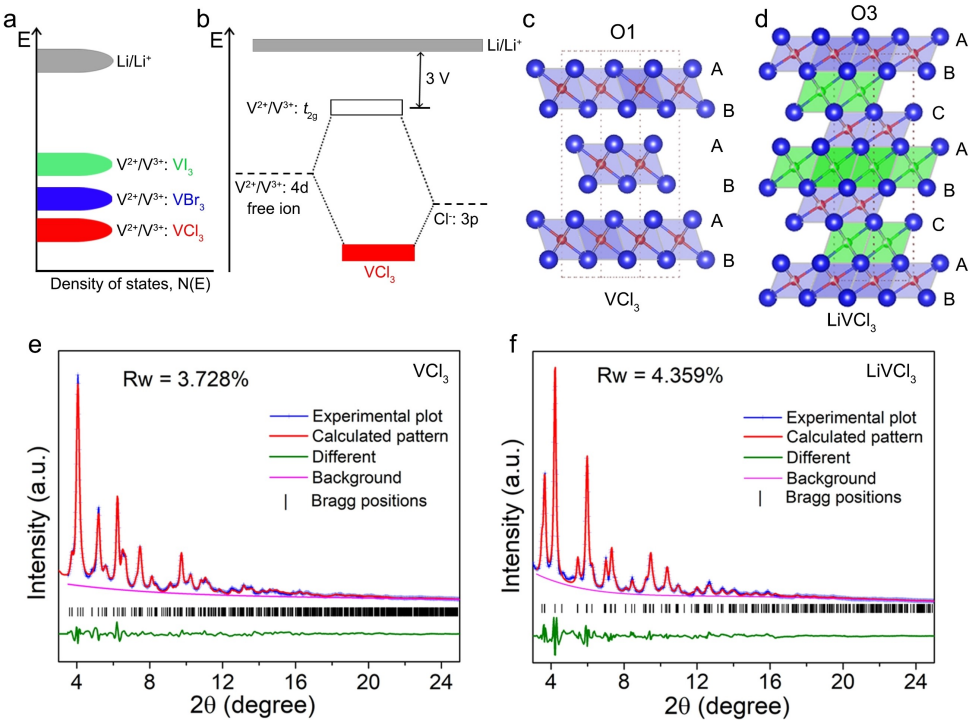

Figure 1. a) The redox energies of the V^{2+}/V^{3+} couple with the influence of the anions. b) Molecular orbital energy diagram illustrating the V^{2+}/V^{3+} redox energy in VCl_3. Crystal structure of c) VCl_3 (the layered O1 structure) and d) $LiVCl_3$ (the layered O3 structure). e), f) The Rietveld refinement results of the synchrotron XRD pattern of e) VCl_3 and f) $LiVCl_3$.

metal, 3*a*, sites of the O3 layered structure with the *R*-3*m* space group. In the case of the stoichiometric $LiVCl_3$ powder, no occupancy of V on the 3*b* sites was observed. Thus, only Li was located on the alkali metal sites. Compared with the VCl_3 structure, the fully lithiated state of $LiVCl_3$ reveals the intercalation of Li in the Van der Waals interlayers, suggesting the potential for good electrochemical performance in a solid-state configuration. Interestingly, such a fully lithiated state of $LiVCl_3$ is different from the reported deficient spinel-type structure of $LiVCl_3$, which can be written as $(Li_{0.79}\square_{0.21})ten.(Li_{0.79}V_{1.21})oct.Cl_4$.[14] Thus, the theoretical lithiation of VCl_3 induces stacking-sequence change from O1 to O3, which is similar to the classical layered oxides (Li_xCoO_2, Li_xNiO_2, etc.).[15]

The electrochemical behaviour of VCl_3 was first evaluated in a homemade solid-state cell using a Li_3InCl_6 SSE (morphology shown in Figure S2). The VCl_3-Li_3InCl_6-C cathode was prepared by mixing VCl_3, Li_3InCl_6, and carbon black in a weight ratio of 5:5:1 (detailed information in Figure S3,4). A thin layer of argyrodite Li_6PS_5Cl SSE was put between Li_3InCl_6 and Li anode to prevent the reduction of the halide Li_3InCl_6 SSE.[16] The d*Q*/d*V* (Figure 2a) and galvanostatic intermittent titration technique (GITT) measurement curves (Figure 2b) indicate two distinct reaction processes with two reduction peaks located at 2.96 V and 2.78 V. The two-step intercalation reactions correspond to $VCl_3 + Li^+ + e^- \rightarrow Li_xVCl_3$, where *x* is the molar ratio of lithium ions inserted to VCl_3. The VCl_3-Li_3InCl_6-C cathode shows a reversible charge capacity of 162.5 mAh g^{-1} at 0.1 C (1 C = 170 mA g^{-1}), corresponding to a high capacity utilization of 95.6 % of the theoretical capacity. Chloride SSEs play an essential role in this chemistry by providing a stable interface with the VCl_3 cathode with no chemical reaction or electrolyte decomposition (Figure S5,6). Other types of SSEs such as sulfide Li_6PS_5Cl SSE was also evaluated. The VCl_3 cathode with the Li_6PS_5Cl SSE shows a low reversible capacity of 105 mAh g^{-1} and a fast capacity fade with a capacity of only 40 mAh g^{-1} remaining after 100 cycles (Figure S7). The poor cycling stability of the VCl_3 cathode in the sulfide system was due to the side reaction between the sulfide SSE and VCl_3 cathode as presented in Figure S6. The quasi-equilibrium potentials presented in the GITT results are consistent with that in the d*Q*/d*V* curves and demonstrate the low overpotential of the VCl_3-Li_3InCl_6-C cathode. The calculated values of the diffusion coefficients (D_{Li^+}) as a function of capacity are displayed in Figure 2c. The high D_{Li^+} values in the range of 10^{-10} cm^2 s^{-1} can be achieved in the whole discharge/charge process, demonstrating the fast kinetics of Li^+ diffusion in the VCl_3-Li_3InCl_6-C cathode.

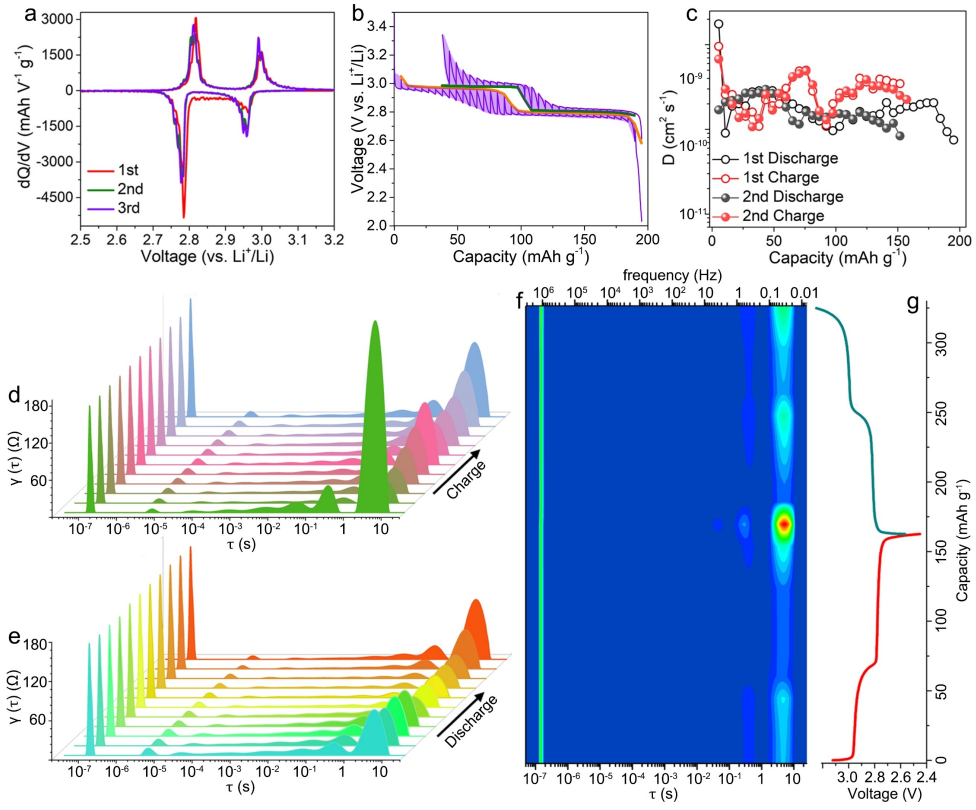

Figure 2. a) d*Q*/d*V* curve of the VCl_3-Li_3InCl_6-C cathode between the potential of 2.45–3.25 V vs. Li^+/Li, obtained at 0.1 C. b) GITT characterization of the VCl_3-Li_3InCl_6-C cathode at the 1st cycle (0.1 C). c) The diffusion coefficients of the VCl_3-Li_3InCl_6-C cathode estimated from GITT measurements. d), e) Distribution of relaxation times (DRT) analysis of the VCl_3-Li_3InCl_6-C cathode cycled at the 2nd cycle (0.1 C). f) Two-dimensional intensity colour map of the DRT curves at the whole discharge-charge process. g) Galvanostatic discharge/charge profiles of the VCl_3-Li_3InCl_6-C cathode at the 2nd cycle (0.1 C).

In situ electrochemical impedance spectroscopy (EIS) was employed to unravel the resistance evolution of the ASSLBs. The impedance spectra during the second lithiation/delithiation process in Figure S8 almost remain stable. Distribution of relaxation time (DRT) analysis was further carried out to probe the change based on the EIS results and the corresponding results are shown in Figure 2d–f. Various processes associated with the cathode and cell properties can be separated and identified in the DRT plots. The peak with the fastest processes above 10^5 Hz is stable without obvious change in intensity during the whole lithiation/delithiation process and should be attributed to the contact impedance between the cathode composites and the current collectors.[17] The peak with the intermediate processes is assumed to the charge transfer behaviour at the interface between the cathode and SSEs.[18] The peak with the slowest processes (with the largest relaxation time) is greatly affected by the lithiation/delithiation states, which is related to the solid-state diffusion of Li^+ ions in the cathode active material.[17a,19] Moreover, Figure 2d–f shows that this peak slightly changed at the beginning and then greatly increases at the end of the lithiation process. Then the peak intensity decreases sharply once delithiation begins. Afterwards, the peak intensity gradually increases until the middle of the delithiation process. A similar initial decrease and then the increasing phenomenon occurred until the fully delithiated state. The evolution should be due to the variation of vacancy and Li^+ content within the Li_xVCl_3 electrode. Li^+ diffusion decreases with the decrease of the vacancy content since more Li^+ sites are occupied during lithiation process.

V K-edge and Cl K-edge X-ray absorption near-edge structure (XANES) spectra of the VCl_3 cathode at different discharge/charge states (Figure 3a, a1–a7) were recorded to reveal the intercalation reaction process (Figure 3d,e). The V K-edge spectra of the commercial VCl_3 and as-synthesized $LiVCl_3$ are presented as references, with distinct features of d1–d4 and d5–d9 observed. During the lithiation process, the XANES spectra features at the a1 state are similar to that of the a2 and the features at the a3 and a4 states are almost the same. A significant change occurs from the a2 to a3 state, demonstrating the structural transition of the active

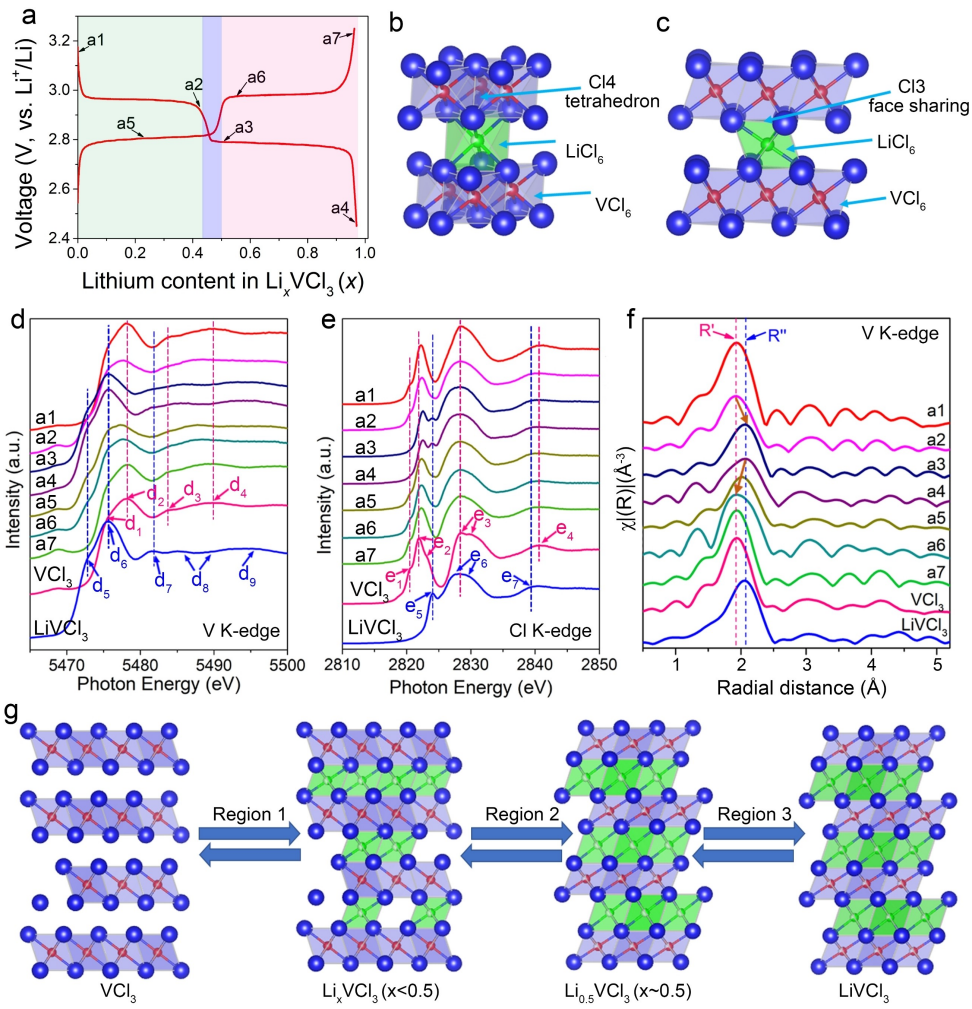

Figure 3. a) Typical discharge/charge curves of VCl_3-Li_3InCl_6-C cathode with 7 selected lithation/delithiation states (a1–a7). b) Lithiated VCl_3 intermediate structure, c) $LiVCl_3$ structure. d) V K-edge, e) Cl K-edge XANES spectra, and f) V K-edge R space EXAFS spectra of the VCl_3-Li_3InCl_6-C cathode collected at the selected lithiation/delithiation state. g) The illustration of the structure evolution of VCl_3 during lithiation/delthiation.

cathode material. Such a structure transition is more obvious reflected from the first shell of V–Cl distance as shown in the V K-edge R space extended X-ray absorption fine structure (EXAFS) spectra (Figure 3f). The XANES spectrum at the fully lithiated state (a4) is the same as the $LiVCl_3$ reference and the shift of the white line from 5478 eV at the a1 state to that of 5475 eV at the a4 state demonstrates the reduction of V^{3+} to V^{2+} (further confirmed by XPS analysis in Figure S9). Then the XANES spectra return to the original state during the re-charge process. The VCl_3 and $LiVCl_3$ also show distinct features for the Cl K-edge spectra (Figure 3e, e1–e4, and e5–e7). The e5 feature ($LiVCl_3$ structure) appears since the a3 state during lithiation and disappears once the beginning of delithiation process. Oppositely, the small pre-edge feature (e1) assigned to the VCl_3 structure disappears since the a3 state while appears again during the delithiation process. The dominant white line (e3 and e6 features) of the Cl K-edge spectra does not show much change, indicating that there is no redox reaction of Cl^- involved during cycling. Thus, as illustrated in Figure 3g, the O1-type layered structure (Figure 3b) of the cathode is preserved in region 1 followed by a structural transition in region 2. Then the O3 layered structure (Figure 3c) appears and remains until the fully lithiated state.

Figure 4a,b shows the rate capability of the VCl_3-Li_3InCl_6-C cathode in the halide SSE system, with a high reversible capacity of 148 mAh g^{-1} achieved at 1 C. Long-term cycling at higher rates of 3 C, 4 C, and 6 C was further performed as presented in Figure 4c. The VCl_3-Li_3InCl_6-C cathode exhibits only minor capacity fade, maintaining 84–85.7 % capacity retention at 3, 4, and 6 C, respectively over 200 cycles. The discharge/charge curves of the cell cycled at 3 C still present two obvious discharge/charge plateaus and a much smaller polarization than that of higher rates (Figure 4d). Figure 4e shows differential capacity curves from

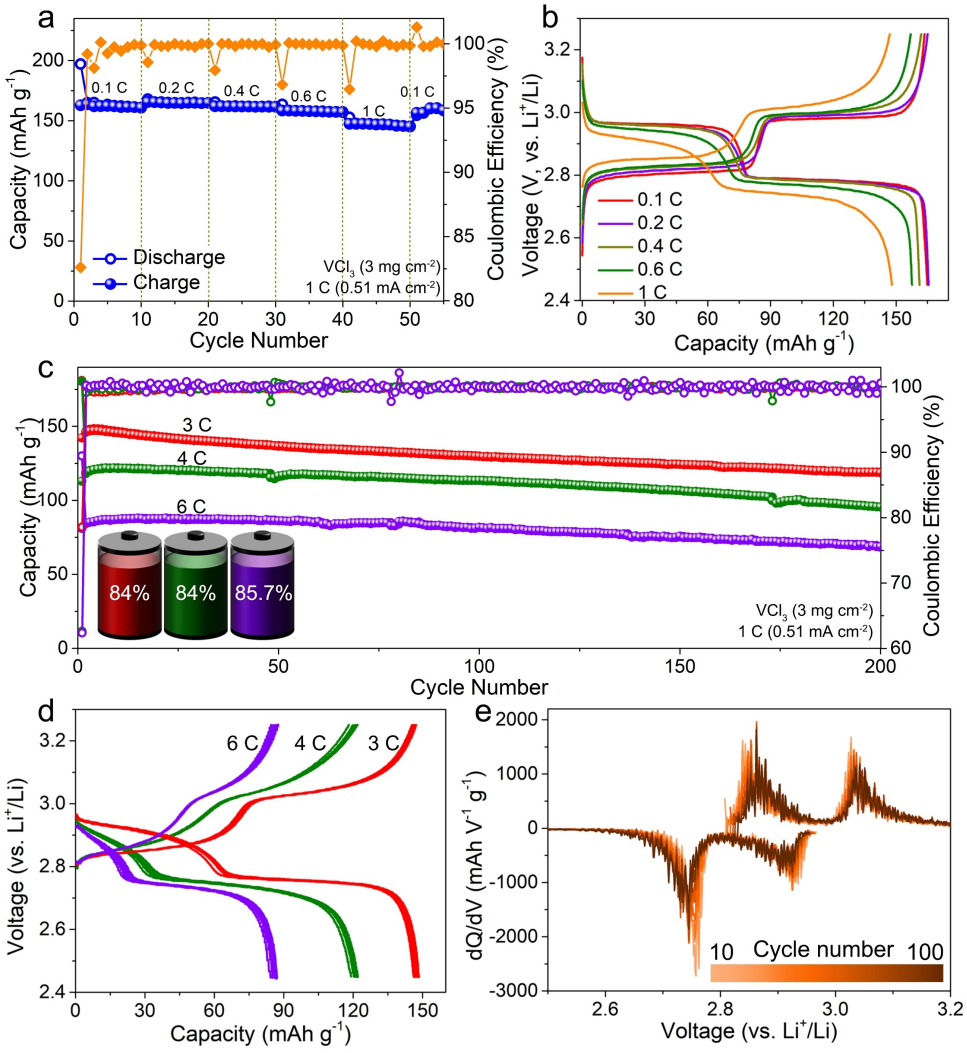

Figure 4. a), d) Discharge/charge capacity as a function of cycle number of the VCl_3-Li_3InCl_6-C cathode from 0.1 C up to 1 C and b) corresponding discharge/charge curves at different C rates for VCl_3. c) Cycling stability of the VCl_3-Li_3InCl_6-C cathode at 3, 4, and 6 C. The battery schemes show the battery's capacity retentions after 200 cycles. d) Discharge/charge curves of the VCl_3-Li_3InCl_6-C cathode at 3, 4, and 6 C from 12nd to 20th cycles. e) d*Q*/d*V* curves of the VCl_3-Li_3InCl_6-C cathode at 3 C during cycling.

cycles 10 to 100 for the same cell at 3 C. Slight changes in the dQ/dV value and voltage can be observed during cycling. The minor shifts in peak position (voltage) demonstrate an increase in resistance over the cycling based on Ohm's law and the flatting of the peak's points to changes in the VCl_3-Li_3InCl_6-C cathode. On the other hand, the lithiation/delithiation behavior of VBr_3 in the vanadium tri-halide family was further investigated (Figure S10,11). Though the reversible capacity is lower than that of VCl_3 (the theoretical capacity of VBr_3 with one molar Li^+ insertion is 127.6 mAh g^{-1}), the cell with the VBr_3-Li3$InCl_6$-C cathode also shows stable cycling performance over 300 cycles. This further suggests that the halide SSEs are suitable electrolytes for layered vanadium tri-halide type insertion cathodes since they eliminate solubility issues and chemical side reactions, which otherwise hinder stable cycling performance.

Given the high ionic conductivity of Li_3InCl_6 at low temperatures ($>10^{-4}$ S cm^{-1} at −25 °C), the ASSLBs were tested at different temperatures from −30 to 60 °C (discharge/charge curves shown in Figure 5a). As presented, the reversible capacities are 167, 162, 117, and 79 mAh g^{-1} at 60, 25, −10, and −30 °C, respectively. It should be noted that the applied current density at 60 °C and 25 °C is 0.4 C, which is higher than that of 0.1 C for −10 °C and −30 °C. The two discharge/charge plateaus can be maintained when the temperature is higher than −10 °C, while large polarization is observed when the cell was cycled at −30 °C. The large polarization at low temperatures should be due to the reduced charge transfer within the cathode composite. Furthermore, the temperature has less impact on the cycling stability of the cells with all the cells exhibiting minor capacity fade (Figure 5b, S12,13). Generally, high temperatures will trigger severe dissolution of electrode materials (such as sulfur) which possess high solubility in a liquid electrolyte. Thus, SSEs with appropriate electrochemical stability windows and good compatibility should be more suitable for these types of electrode materials. The VCl_3 loading was increased to evaluate the performance with high areal capacities. Figure 5c,d shows the results for high-loading VCl_3 ASSBs (25.48 mg cm^{-2} cathode) cycled at 0.2 mA cm^{-2} at room temperature. Though the cell shows higher overpotential under such a high loading, it still delivers stable capacity retention and high specific capacity ($\approx$3 mAh cm^{-2} over 30 cycles). Note that the decreased coulombic efficiency and capacity fade upon cycling should be mainly caused by the anode instability (Figure S14). In addition, the good electrochemical performance of active VCl_3 is not limited to Li_3InCl_6 but also other suitable halide SSEs such as Li_3HoCl_6 as presented in Figure S15–17. Therefore, halide SSEs with high ionic conductivity and wide electrochemical stability windows are promising for the exploring and evaluation of other potential battery intercalation compounds. This opens up the possibility of investigating battery materials with poor compatibility with traditional liquid or other types of solid electrolytes and extending their insertion electrochemistry.

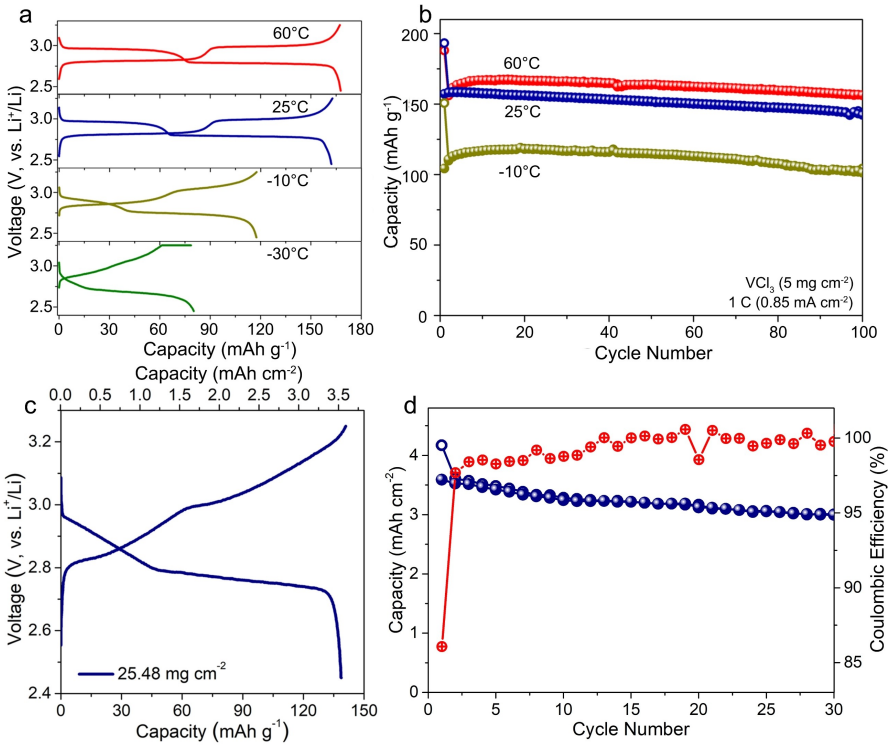

Figure 5. a) Galvanostatic discharge/charge curves at the 2nd cycle and b) cycling performance of the VCl_3-Li_3InCl_6-C cathode at different temperatures. The current density is 0.4 C for 60 °C and 25 °C and 0.1 C for −10 °C. c) Galvanostatic discharge/charge curves and d) cycling performance of the VCl_3-Li_3InCl_6-C cathode at 0.2 mA cm^{-2} with mass loadings of 25.48 mg cm^{-2}.

In summary, a new V^{3+}/V^{2+} chloride cathode was identified in a halide-based solid-state electrolyte system. Its Li^+ insertion and extraction properties were revealed to follow a cationic redox mechanism. The chemical stability between the VCl_3 cathode and halide electrolyte as well as the wide electrochemical stability windows of the halide electrolyte ensures a stable electrode/electrolyte interface and the highly reversible redox reaction of the VCl_3 cathode. The ex situ XANES and EXAFS results revealed the two-step V^{3+}/V^{2+} redox couple in VX_3 during discharge/charge. Fast reaction kinetics and facile Li^+ transport were also achieved as shown by the DRT and GITT results. The all-solid-state battery exhibited a high reversible capacity, excellent rate performance, and long cycle life of over 200 cycles with 85 % capacity retention at 6 C. Moreover, the battery showed good performance at extreme temperatures and ultra-high loading up to 25 $mg\,cm^{-2}$. This work reveals the outstanding potential of lithium-ion insertion electrochemistry in layered halides. Furthermore, our study highlights the significance of the electrode-electrolyte design when searching for new intercalation cathodes for LIBs.

Acknowledgements

This research was supported by Natural Sciences and Engineering Research Council of Canada (NSERC), Canada Research Chair Program (CRC), Canada Foundation for Innovation (CFI), Ontario Research Fund, the Canada Light Source at University of Saskatchewan (CLS), and University of Western Ontario. We also thank Dr. Qunfeng Xiao for helping with the synchrotron measurement.

Conflict of Interest

The authors declare no conflict of interest.

Data Availability Statement

The data that support the findings of this study are available from the corresponding author upon reasonable request.

Keywords: All-Solid-State Battery · Halide Solid Electrolyte · Insertion Electrochemistry · Intercalation Cathode Materials · VCl_3

[1] a) J. B. Goodenough, *Acc. Chem. Res.* **2013**, *46*, 1053–1061; b) M. S. Whittingham, *Chem. Rev.* **2014**, *114*, 11414–11443.
[2] M. S. Whittingham, *Nat. Energy* **2021**, *6*, 214–214.
[3] N. Dubouis, T. Marchandier, G. Rousse, F. Marchini, F. Fauth, M. Avdeev, A. Iadecola, B. Porcheron, M. Deschamps, J. M. Tarascon, *Nat. Mater.* **2021**, *20*, 1545–1550.
[4] a) K. Giagloglou, J. L. Payne, C. Crouch, R. K. Gover, P. A. Connor, J. T. Irvine, *J. Electrochem. Soc.* **2018**, *165*, A3510–A3516; b) N. Tanibata, M. Kato, S. Takimoto, H. Takeda, M. Nakayama, H. Sumi, *Adv. Energy Sustainability Res.* **2020**, *1*, 2000025; c) B. Shao, S. Tan, Y. Huang, L. Zhang, J. Shi, X. Q. Yang, E. Hu, F. Han, *Adv. Funct. Mater.* **2022**, *32*, 2206845.
[5] A. Kajiyama, K. Takada, T. Inada, M. Kouguchi, S. Kondo, M. Watanabe, M. Tabuchi, *Solid State Ionics* **2002**, *152*, 295–302.
[6] a) S. Di Stefano, B. Ratnakumar, C. Bankston, *J. Power Sources* **1990**, *29*, 301–309; b) X. Zhan, M. E. Bowden, X. Lu, J. F. Bonnett, T. Lemmon, D. M. Reed, V. L. Sprenkle, G. Li, *Adv. Energy Mater.* **2020**, *10*, 1903472; c) X. Gao, Y. Hu, Y. Li, J. Wang, X. Wu, J. Yang, Z. Wen, *ACS Appl. Mater. Interfaces* **2020**, *12*, 24767–24776.
[7] a) A. Manthiram, X. Yu, S. Wang, *Nat. Rev. Mater.* **2017**, *2*, 16103; b) A. Banerjee, X. Wang, C. Fang, E. A. Wu, Y. S. Meng, *Chem. Rev.* **2020**, *120*, 6878–6933; c) J. Jang, Y.-T. Chen, G. Deysher, D. Cheng, S.-Y. Ham, A. Cronk, P. Ridley, H. Yang, B. Sayahpour, B. Han, *ACS Energy Lett.* **2022**, *7*, 2531–2539.
[8] C. Yang, J. Chen, X. Ji, T. P. Pollard, X. Lü, C.-J. Sun, S. Hou, Q. Liu, C. Liu, T. Qing, *Nature* **2019**, *569*, 245.
[9] Z. Cheng, H. Pan, F. Li, C. Duan, H. Liu, H. Zhong, C. Sheng, G. Hou, P. He, H. Zhou, *Nat. Commun.* **2022**, *13*, 125.
[10] a) L. Zhou, T.-T. Zuo, C. Y. Kwok, S. Y. Kim, A. Assoud, Q. Zhang, J. Janek, L. F. Nazar, *Nat. Energy* **2022**, *7*, 83–93; b) B. Zahiri, A. Patra, C. Kiggins, A. X. B. Yong, E. Ertekin, J. B. Cook, P. V. Braun, *Nat. Mater.* **2021**, *20*, 1392–1400; c) X. Li, X. Yang, K. Adair, C. Wang, F. Zhao, X. Sun, *Energy Environ. Sci.* **2020**, *13*, 1429–1461; d) J. Liang, X. Li, K. R. Adair, X. Sun, *Acc. Chem. Res.* **2021**, *54*, 1023–1033; e) T. Asano, A. Sakai, S. Ouchi, M. Sakaida, A. Miyazaki, S. Hasegawa, *Adv. Mater.* **2018**, *30*, 1803075.
[11] a) Z. Liu, S. Ma, J. Liu, S. Xiong, Y. Ma, H. Chen, *ACS Energy Lett.* **2021**, *6*, 298–304; b) J. Liang, X. Li, S. Wang, K. R. Adair, W. Li, Y. Zhao, C. Wang, Y. Hu, L. Zhang, S. Zhao, *J. Am. Chem. Soc.* **2020**, *142*, 7012–7022.
[12] a) X. Li, J. Liang, N. Chen, J. Luo, K. R. Adair, C. Wang, M. N. Banis, T.-K. Sham, L. Zhang, S. Zhao, S. Lu, H. Huang, R. Li, X. Sun, *Angew. Chem. Int. Ed.* **2019**, *58*, 16427–16432; *Angew. Chem.* **2019**, *131*, 16579–16584; b) K. Wang, Q. Ren, Z. Gu, C. Duan, J. Wang, F. Zhu, Y. Fu, J. Hao, J. Zhu, L. He, C.-W. Wang, Y. Lu, J. Ma, C. Ma, *Nat. Commun.* **2021**, *12*, 4410.
[13] a) C. Wang, J. Liang, M. Jiang, X. Li, S. Mukherjee, K. Adair, M. Zheng, Y. Zhao, F. Zhao, S. Zhang, *Nano Energy* **2020**, *76*, 105015; b) C. Wang, R. Yu, H. Duan, Q. Lu, Q. Li, K. R. Adair, D. Bao, Y. Liu, R. Yang, J. Wang, S. Zhao, H. Huang, X. Sun, *ACS Energy Lett.* **2022**, *7*, 410–416.
[14] J. Soubeyroux, C. Cros, W. Gang, R. Kanno, M. Pouchard, *Solid State Ionics* **1985**, *15*, 293–300.
[15] M. D. Radin, J. Alvarado, Y. S. Meng, A. Van der Ven, *Nano Lett.* **2017**, *17*, 7789–7795.
[16] W. Ji, D. Zheng, X. Zhang, T. Ding, D. Qu, *J. Mater. Chem. A* **2021**, *9*, 15012–15018.
[17] a) X. Chen, L. Li, M. Liu, T. Huang, A. Yu, *J. Power Sources* **2021**, *496*, 229867; b) X. Zhou, Z. Pan, X. Han, L. Lu, M. Ouyang, *J. Power Sources* **2019**, *417*, 188–192.
[18] C. Sheng, F. Yu, C. Li, H. Zhang, J. Huang, Y. Wu, M. Armand, Y. Chen, *J. Phys. Chem. Lett.* **2021**, *12*, 2064–2071.
[19] P. Gargh, A. Sarkar, Y. H. Lui, S. Shen, C. Hu, S. Hu, I. C. Nlebedim, P. Shrotriya, *J. Power Sources* **2021**, *485*, 229360.

Manuscript received: November 21, 2022
Accepted manuscript online: January 25, 2023
Version of record online: February 16, 2023